Modeling Mechanical Behaviors of Plant Stems undergoing Microstructural Changes

Ruyue Song and Anastasia Muliana*
Department of Mechanical Engineering, Texas A&M University
*Corresponding author: amuliana@tamu.edu

Abstract

This study presents a constitutive material model for describing nonlinear and hysteretic responses of plant tissues subjected to mechanical loadings. The nonlinear and hysteretic response is associated with the viscoelastic nature of the constituents and microstructural changes of plant tissues during loadings. In order to incorporate the effect of microstructural changes on the macroscopic response of plant tissue, we assume that as the tissue is deformed, an additional micromechanism arises affecting the mechanical response of the tissues. The plant tissue is assumed to consist of two networks, the initial network which is associated with an original reference configuration and the new network that is formed during the deformation. The newly formed network has a new natural configuration. The responses obtained from the proposed model are compared with available experimental data of plant tissues. The model is easily extended to incorporate responses of different tissues, i.e., outer strengthening skin and inner soft core, in determining the overall nonlinear behaviors of the plant stems, which are composite materials. Thus, we can examine the contributions of different constituents in the plant tissues on their macroscopic mechanical responses.

Introduction

Plant stems compose of various constituents and arrangements of microstructural morphologies that are well integrated, forming hierarchical structures. Their unique hierarchical structures, which are developed during growth, allow them to perform multiple functions, such as adaptation to various environmental and mechanical conditions for survivability and reproduction, load bearing to different mechanical stimuli (i.e., wind, touch and rain), self-regulating energy from multiple sources (sun-light, water, mineral), self-healing of damage tissues, etc. Detailed discussions of the hierarchical structures of plant stems can be found in Niklas (1992), Speck and Burgert (2011) and Brulé et al. (2016).

In this study, we focus our attention on the mechanical response of plant tissues particularly on their nonlinear and hysteretic responses that are observed at the macroscopic scale. Understanding the mechanical response of plant stems is often done by performing laboratory testing under different boundary conditions, such as bending, tension, compression, twisting, buckling, etc. Information on the overall elastic modulus, stiffness, failure load- and mechanism are typically recorded and correlated to the morphologies of the stems (Gibson (2012), Robertson et al. (2017), Robertson et al. (2016), Gomez et al. (2017), Gomez et al. (2018), Shah et al. (2017)). The macroscopic responses of plant stems under mechanical loadings, often reported in terms of stress-strain relations, are a manifestation of continuous changes and interactions of different microstructural morphologies and constituents within the stems. It is also noted that the living plant's responses to mechanical loadings will involve multiple enzymes and biochemical processes, in addition to the physical microstructural changes. For example in their study Park and Cosgrove (2012) mentioned that a digestion of enzymes between cellulose microfibers should influence the mechanical behaviors of the cell walls. In this study we focus mainly on capturing the overall

(macroscopic) mechanical response of plant tissues due to the net effect of changes in the microstructural morphologies. Our aim is not on incorporating the precise microstructural models, instead we are considering a phenomenological approach with internal state variables to incorporate microstructural evolution which can be directly correlated to macroscopic experimental tests discussed above. Within the phenomenological approach, the internal state variable can still incorporate the physical information of the microstructural changes.

There have been several experimental studies on investigating changes in the microstructures of plant tissues under mechanical loadings. Burgert (2006) discussed that the mechanical response of plant cell walls is strongly correlated to the cellulose micro-fibril orientations and to the interaction between cellulose fibers and soft matrix. When subjected to a mechanical loading, the fibers in the cell walls tend to reorient themselves in order to adjust their stiffness and toughness to the external stimulus. It has also been shown that different fiber orientations distinguish the flexible and stiff cell walls in young and adult woods, respectively (Lindström et al. (1998), Lichtenegger et al. (1999)). Scanning electron microscopy and X-ray scattering measurements indicate that straining the cell walls induces microstructural changes, such as reorientations of micro-fibril angles and fiber-matrix separations, which at the macroscopic scale are translated to nonlinear and inelastic stress-strain relations (Köhler and Spatz 2002). The extent of fiber reorientations and fiber-matrix separations depends on the amount of straining induced on the cell walls. It should be noted that most of the microscopic measurements were done postmortem, and thus detailed evolutions of the physical changes in the microstructures during mechanical loadings are largely unexplored.

The process of microstructural changes dissipates energy, which at the macroscopic scale is observed by a hysteretic response. The microstructural changes often result in a permanent set

if upon removal of the external stimuli the material does not regain its original microstructures. For examples, several studies suggested that sliding between fibers or a fiber-matrix separation results in permanent microstructural changes, and hence permanent deformations. Köhler and Spatz (2002) showed that the permanent deformation in cell walls due to a tensile loading is associated with the changes in the fiber angle orientation from its original orientation. Plant tissues also exhibit viscoelastic responses when subjected to mechanical loadings, e.g., Salmen (1984); Spatz et al. (1999); Köhler and Spatz (2002); Speck and Spatz (2003), Kerstens et al. (2001); Hogan and Niklas (2004); Hayot et al. (2012), and Lee et al. (2019). These viscoelastic responses are associated with the polymer building blocks of the fibers and matrix, i.e., cellulose, hemicellulose, and lignin, with long chain and multiple network microstructures. Their macromolecular networks lead to viscoelastic behaviors when they are subjected to mechanical loadings. In living tissues, the existence of fluid can also amplify the viscoelastic response of the stems. An experimental study by Salmen (1984) indicated that woods tested along and across the fiber directions experienced different viscoelastic responses, with more pronounced response in the across fiber direction. The lignin matrix dominates the mechanical response of woods when they are loaded across the fiber axis, while loading along the fiber axis is dominated by the fiber behaviors. This indicates that the lignin shows more pronounced viscoelastic response compared to the cellulose fibers. Köhler and Spatz (2002) tested a sclerenchyma tissue under several loading-unloading cycles at different rates. They observed that the energy loss in the hysteretic loops depends on the loading rates, which is not surprising considering the viscoelastic nature of the biological tissue. The energy loss was modeled with dry and viscous frictions since considering the viscous friction alone was not sufficient in quantitatively predicting the amount of the energy loss. They discussed that the hysteretic inelastic deformations were related to breaking and

reforming of hydrogen bonds between the cellulose fibrils. When the bonds break during loading, viscous flow occurred in the matrix, and unloading caused formations of new bonding, and hence new fibril configurations. However, it is not clear what mechanisms were associated with the dry friction as this component was added to match the experimental data.

There have been several approaches in modeling the nonlinear inelastic response of plant cell walls. Fratzl et al. (2004) and Altaner and Jarvis (2008) considered a 'molecular Velcro' model to describe a stick-slip mechanism between the cellulose micro-fibril and hemicellulose matrix. During loadings, combined normal and shear strains induced detachments of the cellulose fibrils from the matrix and sliding between micro-fibrils. Upon unloading, the cellulose fibrils were reattached to the matrix, but slipping was unrecoverable, leading to inelastic deformations. The model, however, did not account for possible reorientation of fibril angles due to loading, and the quality of the model in capturing unloading and possible reloading stages has not been assessed. Navi et al. (1995) and Navi and Sedighi-Gilani (2004) used a micromechanics approach to incorporate the elastic moduli of cellulose fibrils, lignin matrix, and fibril reorientations in explaining the nonlinear inelastic response of cell walls. They assumed that increasing the tensile force decreased the microfibril angles as they oriented towards the loading direction and damaged the surrounding matrix. The orientation of microfibrils towards loading axis caused stiffening behaviors and damage in the matrix resulted in permanent deformation. However, the model did not capture the possible hysteretic loops of the unloading-reloading paths nor included the time-dependent behaviors. Borodulina et al. (2015) proposed a micromechanics model that incorporates a linear elastic behavior of cellulose microfibril and an elastic-plastic behavior of matrix, comprising of lignin and hemicellulose. The tensile load induced microfibril reorientations. The proposed approach was capable in capturing the nonlinear hysteretic response of the fibers and the

effect of microfibril angles on the overall deformations. Trivaudey et al. (2015) proposed a constitutive model for describing a nonlinear tensile behavior of hemp fibers. The model incorporated the viscoelastic response, microfibril reorientation, and shear induced crystallization of the amorphous components. The model showed its ability in capturing the creep and nonlinear tensile behaviors of the tested specimens. This approach is based on several hypotheses made in describing the nonlinear mechanical response of plant tissues, which may be applicable for specific tissues. In order to gain confident in the material parameters and hypotheses discussed in the model, it will require extensive testing at the microscopic scale and/or the ability to track continuous changes of the microstructures during testing; otherwise the approach can be seen as mainly curve fitting parameters. Unfortunately, the authors did not present a complete hysteretic response to further examine the validity of their model and hypotheses. Another micromechanical model proposed to describe the nonlinear inelastic response of plant tissues in by Pieczywek and Zdunek (2014). The authors modeled detailed cell wall geometries of the onion epidermis tissue and incorporating elastic-plastic constitutive model for the cell wall. The model is shown capable in capturing the loading response; however there have been no discussion on the unloading-reloading response to further examine the model. Similar to the approach in Pieczywek and Zdunek (2014), Singh et al. (2013) and Zhu and Melrose (2003) modeled plant cell walls with honeycomb lattice structures and used hyperelastic constitutive models to describe the overall nonlinear response of cell walls. Using hyperelastic constitutive model will not allow for capturing the hysteretic response and possible permanent deformation.

To our knowledge, there has not been any phenomenological model used to describe nonlinear, hysteretic, time-dependent, and inelastic response of plant tissues. There are several nonlinear, time-dependent, and inelastic phenomenological models formulated for polymers and

metals. These phenomenological models often have large numbers of material parameters which require multiple mechanical testing to calibrate them. Some of them involve parameters that are specifically applied for polymers or metals, e.g., burger vector, chain entanglement, etc., making it difficult to use the models for plant tissues.

In summary, experimental tests on various plant tissues show nonlinear, hysteretic, inelastic and time-dependent mechanical behaviors at the macroscopic scale. Limited microscopic measurements indicate that multiple microstructural changes can take place, depending on the loading types and histories. The loading-unloading of the cell wall imposes reorientations of the microfibril angles between the initial orientation and the loading axis. These microfibril reorientations induce deformations and stresses to the surrounding matrix, and it is also possible for the microfibrils to undergo elongation and failure. Both cellulose microfibrils and matrix are polymers with long chain and multiple network microstructures. When subjected to mechanical loadings they exhibit viscoelastic behaviors due to the rearrangements of the long macromolecular chains. Depending on the extent of loadings and characteristics of macromolecular networks, irreversible changes in the macromolecular networks of the microfibrils and matrix can occur, leading to a macroscopic permanent set. As discussed above, several microstructurally motivated models have been proposed to describe the nonlinear hysteretic responses of plant tissues under mechanical loadings. Some of these micromechanically motivated models are based on specific hypotheses which might be applicable for specific tissues under certain loading conditions. Some other micromechanically motivated models consider only one or a few mechanisms, neglecting other possible mechanisms. In addition, most of these models mainly capture the nonlinear responses during loading without discussing the hysteretic response and possible formation of permanent deformations. It might be possible to formulate micromechanics models that

incorporate precise physical mechanisms associated to the nonlinear hysteretic responses when the continuous evolution of the microstructures due to loadings can be measured experimentally.

The motivation of this study is to be able to capture a complete nonlinear hysteretic and time-dependent response and predict permanent deformations of plant tissues subjected to various histories of loading, e.g., ramp, creep, cyclic, etc. We consider a constitutive model that includes the effect of microstructural changes in describing the macroscopic response of the tissues. The main highlight of the model is that it has a few material parameters that can be calibrated easily from available macroscopic experimental data. As will be shown later, the material parameters in the constitutive model have physical representations, i.e., stiffness and viscosity. The model treats the plant tissue as a homogenized medium, and the net effect of possible microstructural changes, such as fibril reorientations, viscoelastic behaviors of fibers and matrix, possible sliding between fibers and fiber-matrix, etc., is incorporated through introducing an internal state variable. It is noted that in many biomechanics studies of plant tissues, several mechanical properties, such as elastic modulus, yield stress, failure deformation, etc., are obtained from testing tissues at a relatively large scale, which are inherently phenomenological properties determined by treating the plant tissues as homogenized bodies. Furthermore, our motivation in predicting the overall nonlinear hysteretic and time-dependent response is to be able to understand structural failure (lodging) in plant stems under mechanical loading, such as wind at different speeds and multiple cycles. Such an understanding can eventually help plant breeders in selecting lodging resistant variants.

A constitutive model for nonlinear hysteretic and time-dependent responses of plant tissues

This section discusses a new constitutive material model of plant tissues undergoing microstructural changes. In deriving the model, we adopt a multiple natural configuration approach. The natural configuration is considered when the material is under a stress-free state. We consider the plant tissues as being composed of two microstructural networks, the original network and the new network formed due to prescribing mechanical loadings. For an illustration purpose, **Figure 1a** depicts an example of a macroscopic stress-strain of a plant tissues under a mechanical loading, i.e., uniaxial tension. The overall deformations of the plant tissues are attributed to the deformations of the cell walls. At its initial stage, it is assumed that the cell wall is under stress- and strain free conditions[1]. When an applied loading is relatively small, the stress-strain shows a nearly linear response and upon unloading – given a sufficient recovery time – the response returns to the initial stress-strain free stage. The macroscopic response at this state of loading is associated with a specific microstructural morphology of the cell wall (original network), referred as an initial configuration. **Figure 1b** illustrates a cartoon of a simplified cell-wall microstructure at several scales, at an initial configuration[2]. Corresponding to the initial microstructural configuration, the tissue has overall (homogenized) mechanical and physical properties, i.e., modulus of elasticity, viscosity, permeability, etc. Prescribing a relatively large mechanical loading can induce significant changes in the microstructural morphology of the cell walls, e.g., fiber reorientation, realignment of macromolecular network, matrix damage, fiber breaking, etc. At this stage it is assumed that a new network is being formed. When upon removal of the load a permanent

[1] The cell wall can be under stresses, for example from a turgor pressure, even when the external mechanical loading is absent. In this study, the initial configuration is attributed to a configuration at which the mechanical loading is initially prescribed.

[2] This illustration is not meant to describe precise microstructural morphologies, as the real morphologies and their changes due to loadings are far more complex than the ones illustrated in the figure. The figure is used to motivate the idea of a microstructural changes in describing the macroscopic nonlinear hysteretic response of plant cell wall.

deformation is observed, it is said that the tissue has a different microstructural configuration (intermediate state) than the one of the initial configuration. A different microstructural configuration at this intermediate state will yield to different overall mechanical and physical properties than the ones at the initial configuration. We further assume that there is a final configuration, at which a complete microstructural change has taken place (no further changes are possible, all tissue is comprised of the newly formed network). At this final configuration, the tissue has the associated mechanical and physical properties that may differ than the properties at the initial and intermediate configurations. For example, experimental studies have indicated that the elastic modulus of a cell wall depends on the microfibril angle and experimental studies have also suggested that deformations induce reorientations of microfibril angle. Thus, as the microstructural morphology of the cell wall changes with loading, its mechanical and physical properties also change. Prescribing continuous loading will then induce continuous microstructural changes. In order to incorporate the effect of continuous microstructural evolution on the macroscopic response of plant tissue, we introduce an internal state variable α that accounts for the net microstructural changes between the two configurations[3]. The value of α is between 0 and 1, referring to the initial and final configurations, respectively. When α=0, the cell wall has an initial microstructural morphology (original network); for α=1 the cell wall has the final microstructural morphology (new network); and when $0 < \alpha < 1$ the cell wall has a combination of initial and final microstructural morphologies with α indicates a fraction of the new network

[3] The microstructural changes in plant tissue due to mechanical loadings are often associated with multiple mechanisms and the internal state variable α is used to quantify the fraction of net changes. However, in case a single dominant mechanism associated with the mechanical loading can be identified, e.g., microfibril orientation, the parameter α now has a physical measure which quantifies changes in the microfibril orientation from the initial orientation θ_0 (α=0) to the maximum orientation, i.e., loading axis in case tension is prescribed (α=1). Thus, the microfibril orientation can only occur between these two orientations. Changes in the internal state variable α will depend on the extent of prescribed mechanical loadings, which will be discussed later.

being formed. We will examine whether this proposition can give a reasonable approximation in describing the nonlinear and hysteretic response of plant cell wall.

We derive the constitutive model from a thermodynamics of a continuous body. We adopt the theory of multiple natural configurations that has been used to model responses of materials undergoing microstructural changes, e.g., (Rajagopal and Wineman (1992); Rajagopal and Srinivasa (2004); de Tommasi et al. (2006) and (2010); Muliana et al. (2016); Xing et al. (2017); Yuan et al. (2017); Song et al. (2018) and (2019)). In the de Tommasi et al. (2010), the authors considered damage and self-healing in spider silks by taking into account breaking of the hydrogen bonds, as the internal state variable, in the materials that lead to softening and reforming of the bonds in case of healing. Since we are relying on data in literature, which use the engineering stress-strain measures, to examine the quality of our model, we present the model in terms of the engineering stress-strain measure. Here we present a one-dimensional model since the currently available data in literature mainly report stress-strain along the loading axis. However, the model is general and was derived for multiaxial cases. **Appendix A** briefly summarizes a three-dimensional model representation. In the three-dimensional model, there are additional material parameters which can only be calibrated by performing multi-axial experimental tests.

Consider a plant tissue comprising of two networks, and each network has a distinct microstructure. Initially the tissue consists of one network (the original network) and as the deformation takes place microstructural changes occur and a new network is being formed. These networks have their own "natural configuration". Each network has two distinct energy storage mechanisms and a dissipation mechanism, we refer to the elastic component (N) for the one that can only store energy and viscoelastic (V) component for the one that can store and dissipate energy.

The Gibbs free energy is of the form $G = G(\sigma_V, \sigma_N, \alpha)$, and the Helmholtz free energy and its rates are:

$$\psi = G - \frac{\partial G}{\partial \sigma_V}\sigma_V - \frac{\partial G}{\partial \sigma_N}\sigma_N \tag{1}$$

$$\dot{\psi} = \frac{\partial G}{\partial \alpha}\dot{\alpha} - \frac{d}{dt}\left(\frac{\partial G}{\partial \sigma_V}\right)\sigma_V - \frac{d}{dt}\left(\frac{\partial G}{\partial \sigma_N}\right)\sigma_N \tag{2}$$

We assume that the elastic and viscoelastic components produce the same strain. The 'reversible' strain ε_e is written as:

$$\varepsilon_e = \varepsilon_V = \varepsilon_N \tag{3}$$

Within the viscoelastic part, we have the elastic recovery and dissipative parts:

$$\varepsilon_V = \varepsilon_V^e + \varepsilon_V^d \tag{4}$$

where

$$\varepsilon_V^e = -\frac{\partial G}{\partial \sigma_V} \rightarrow \dot{\varepsilon}_V^e = -\frac{d}{dt}\left(\frac{\partial G}{\partial \sigma_V}\right) = \dot{\varepsilon}_e - \dot{\varepsilon}_V^d \tag{5}$$

The total strain in the body is assumed to be the superposition of the reversible viscoelastic strain and the permanent strain due to the microstructural change:

$$\varepsilon = \varepsilon_e + \varepsilon_p = \varepsilon_e + \alpha\varepsilon_{\max} \tag{6}$$

where the permanent strain is assumed to be proportional to microstructural change, and $\varepsilon_{\max}$ is the maximum permanent strain. The overdot in Eqs. (2) and (5) denotes the time derivative. It is also noted that the stress is an additive decomposition of the elastic and viscoelastic parts: $\sigma = \sigma_N + \sigma_V$.

Next, we define the rate of the mechanical dissipation:

$$\xi = \sigma\dot{\varepsilon} - \dot{\psi} \tag{7}$$

Substituting Eqs. (2)-(6) into Eq. (7) gives:

$$\xi = \sigma_V \left(\dot{\varepsilon} - \dot{\varepsilon}_p - \dot{\varepsilon}_V^d \right) + \sigma_N \left(\dot{\varepsilon} - \dot{\varepsilon}_p \right) - \frac{\partial G}{\partial \alpha} \dot{\alpha} = \sigma_V \dot{\varepsilon}_V^d + \left(\sigma \varepsilon_{\max} - \frac{\partial G}{\partial \alpha} \right) \dot{\alpha} \tag{8}$$

We consider the following form of the Gibbs potential:

$$G(\sigma_V, \sigma_N, \alpha) = -\left(\frac{\alpha \sigma_V^2}{2E_{Vf}} + \frac{(1-\alpha)\sigma_V^2}{2E_{Vo}} \right) - \left(\frac{\alpha \sigma_N^2}{2E_{Nf}} + \frac{(1-\alpha)\sigma_N^2}{2E_{No}} \right) \tag{9}$$

The above potential gives the following constitutive equations for the elastic and viscoelastic parts:

$$\varepsilon_N = -\frac{\partial G}{\partial \sigma_N} = \frac{\alpha \sigma_N}{E_{Nf}} + \frac{(1-\alpha)\sigma_N}{E_{No}} \tag{10}$$

$$\varepsilon_V = \varepsilon_V^e + \varepsilon_V^d = -\frac{\partial G}{\partial \sigma_V} + \varepsilon_V^d = \frac{\alpha \sigma_V}{E_{Vf}} + \frac{(1-\alpha)\sigma_V}{E_{Vo}} + \varepsilon_V^d \tag{11}$$

$$\dot{\varepsilon}_V^d = \left(\frac{\alpha}{\mu_f} + \frac{1-\alpha}{\mu_o} \right) \sigma_V \tag{12}$$

From Eqs. (9)-(12) we can see that there are three material parameters involved, which are moduli for the elastic and viscoelastic parts and viscosity for the viscoelastic part. They are referred as E_N, E_V, μ, respectively. These material parameters evolve with the mechanical loading. Thus, with regards to the initial and final microstructural configurations, we have the following material parameters: $E_{No}, E_{Vo}, \mu_o, E_{Nf}, E_{Vf}, \mu_f$. Equation (9) represents the stored energy from the elastic and viscoelastic responses. Recall the mechanical dissipation in Eq. (8), and with the Gibbs potential in Eq. (9), we have:

$$F = \sigma \varepsilon_{\max} - \frac{\partial G}{\partial \alpha} = \sigma \varepsilon_{\max} + \left(\frac{\sigma_D^2}{2E_{Df}} - \frac{\sigma_D^2}{2E_{Do}} \right) + \left(\frac{\sigma_N^2}{2E_{Nf}} - \frac{\sigma_N^2}{2E_{No}} \right) \tag{13}$$

Equation (13) is the driving force for the microstructural changes. It is noted that it is necessary for the rate of mechanical dissipation in Eq. (8) to be non-negative and that $F\dot{\alpha} \geq 0$.

In many cases, experimental data pertinent to the time-dependent response of plant tissues are not being reported. In order to capture the nonlinear hysteretic response, in absence of the viscous dissipation, we can reduce the above model by eliminating $\dot{\varepsilon}_D^v$ (letting $\frac{1}{\mu_i}=\frac{\alpha}{\mu_f}+\frac{(1-\alpha)}{\mu_o}=0$). Thus, according to Eqs. (3)-(4) and (9)-(10), the reversible part of the model reduced to an elastic response with a modulus of elasticity as a material parameter. The only stress involved is σ and the elastic moduli at the initial and final configurations become $E_o=E_{Vo}+E_{No}$ and $E_f=E_{Vf}+E_{Nf}$, respectively. Thus, the Gibbs potential in Eq. (9) reduces to:

$$G(\alpha,\sigma)=-\left(\frac{\alpha\sigma^2}{2E_f}+\frac{(1-\alpha)\sigma^2}{2E_o}\right) \tag{14}$$

The parameters E_o and E_f are the material stiffness at the initial configuration (α=0) and final configuration (α=1), respectively. Following a standard procedure in imposing the thermodynamics relations, the rate of the mechanical dissipation is

$$\xi=\sigma\dot{\varepsilon}_p-\frac{\partial G}{\partial\alpha}\dot{\alpha}=\sigma\left(\dot{\varepsilon}-\dot{\varepsilon}_e\right)-\frac{\partial G}{\partial\alpha}\dot{\alpha} \tag{15}$$

where the reversible strain, defined as the superposition of elastic strains of the two configurations, can be derived from the Gibbs free energy:

$$\varepsilon_e=-\frac{\partial G}{\partial\sigma}=\frac{\alpha\sigma}{E_f}+\frac{(1-\alpha)\sigma}{E_o} \tag{16}$$

It is seen in Eq. (16) that at the intermediate state, the elastic modulus E_i is given as $\frac{1}{E_i}=\frac{\alpha}{E_f}+\frac{(1-\alpha)}{E_o}$. The rate of dissipation associated with the microstructural changes are expressed in Eq. (15). The term $\sigma\left(\dot{\varepsilon}-\dot{\varepsilon}_e\right)$ is related to the permanent strain due to microstructural

changes. As discussed above, we need to satisfy the constraint $\xi \geq 0$, and we also need to define the evolution of the microstructural changes due to the deformation. These will be discussed later during the material characterization from available experimental data.

Finally, the total energy dissipation is defined as:

$$W_d = \oint \xi dt \geq 0 \tag{17}$$

Material Parameter Characterization from Experimental Data

In this section we discuss the determination of material parameters in the above model from the nonlinear hysteretic response of plant tissues. For this purpose, we first used data of wet wood tissue of spruce (*Picea abies*), provided by Burgert (2006). The data were discussed for time-independent response, thus we eliminate the viscous dissipation part and use the Gibbs potential given in Eq. (14). Before we proceed with the material parameter characterization, we need to identify the relation between the evolution of the microstructural changes and the deformation. Figure 2 shows the hysteretic response of the tested wet wood tissue of spruce. It is seen that multiple loading-unloading cycles lead to a sequence of permanent deformations, which are associated with changes in the microstructures of the plants. While these changes can occur at multiple scales, the proposed approach considers the net effect of the microstructural changes. The unloading-reloading cycles also show significant hysteretic loops.

The material modulus at the initial configuration (original network), E_o, is calibrated by taking the slope the initial loading (zero stress-strain), while the modulus at the final configuration (new network) E_f is calibrated at the maximum unloading strain, where a complete microstructural change has taken place, $\alpha \approx 1$. It is assumed that the permanent strain is proportional to the extent of microstructural change α:

$$\varepsilon - \varepsilon_e = \alpha\varepsilon_{\max} \rightarrow \left(\dot{\varepsilon} - \dot{\varepsilon}_e\right) = \dot{\alpha}\varepsilon_{\max} \tag{18}$$

where $\varepsilon_{\max}$ is the maximum remanent strain, as depicted in Figure 2. The value for $\varepsilon_{\max}$ is calculated by using the maximum strain minus the reversible part of the strain at the maximum load. The calibration results for the wet wood tissue of spruce are $E_o = 1.189GPa$, $E_f = 1.757GPa$ and $\varepsilon_{\max} = 13.65\%$. From Eqs. (16) and (18), the strain is given as:

$$\varepsilon = \frac{\alpha\sigma}{E_f} + \frac{(1-\alpha)\sigma}{E_o} + \alpha\varepsilon_{\max} \tag{19}$$

The rate of energy dissipation in Eq. (15) can now be written as:

$$\xi = \sigma\dot{\varepsilon}_p - \frac{\partial G}{\partial \alpha}\dot{\alpha} = \sigma\varepsilon_{\max}\dot{\alpha} - \frac{\partial G}{\partial \alpha}\dot{\alpha} = F\dot{\alpha} \tag{20}$$

where F is the driving force for the microstructural changes due to mechanical loading. The expression of F is:

$$F = \sigma\varepsilon_{max} - \frac{\partial G}{\partial \alpha} = \sigma\varepsilon_{max} + \sigma^2\left(\frac{1}{2E_f} - \frac{1}{2E_o}\right) \tag{21}$$

Since at the initial stage (α=0 and σ=0), the microstructural changes have not yet taken place and F=0. Also from Eq. (19), the microstructural change is explicitly expressed as:

$$\alpha = \frac{\varepsilon - \dfrac{\sigma}{E_o}}{\dfrac{\sigma}{E_f} - \dfrac{\sigma}{E_o} + \varepsilon_{max}} \tag{22}$$

Now in order to examine the relation between the driving force F and microstructural changes α, we plot the outer loop of the hysteretic response, shown in Figure 3. Once the parameters $E_o, E_f, \varepsilon_{\max}$ have been determined, the experimental plot of F-α can be constructed from Eqs. (21) and (22). It is seen in Figure 3(bottom) we can form a relationship between F-α. We then

mathematically describe the F-α relationship. This can be done by picking suitable functions to capture the entire F-α relationship from the outer loop in Figure 3(bottom). An alternative approach is to use a weighted superposition of kernels of the Preisach-Krasnoselskii operator, which is described in Mayergoyz (1986), (2003). The Preisach-Krasnoselskii approach describes a phenomenological hysteretic model of any physical behavior. In this study, we consider the Preisach-Krasnoselskii operator and need to determine number of hysteron used in the operator, in which we use the outer loop data of the F-α curve. The number of hysteron describes the smoothness of the response, as discussed in **Appendix B**. In this study the number of hysteron N=5050 is used. The material parameters are summarized in Table 1. When suitable mathematical functions are used to describe the F-α curve, we can also capture the overall hysteretic response, as discussed in **Appendix C**.

The hysteretic response of a plant cell wall with microstructural changes is then determined from Eqs. (19) and (21), and F-α relationship through the use of the Preisach-Krasnoselskii operator. Finally, we show the prediction of the stress-strain hysteretic response of a wet wood tissue of spruce (*Picea abies*), tested by Burgert (2006), in Figure 4. Overall the model that incorporate a continuous evolution of the microstructure with deformations is capable of capturing the entire hysteretic response.

We also test the approach using a hysteretic response of a different plant tissue. We consider an isolated sclerenchyma tissue of *Aristolochia macrophylla* tested by Köhler and Spatz (2002). The same procedure as discussed above is used to calibrate the material parameters in the model, which are listed in Table 1. Figure 5 shows the simulation results for isolated sclerenchyma tissue of *Aristolochia macrophylla*. For both cyclic and quasi static responses, the model gives a reasonably good prediction compared to the experimental result.

Investigation of the Effect of Viscoelasticity on the Hysteretic Response

Köhler and Spatz (2002) discussed the viscoelastic effect in the overall hysteretic response of the isolated sclerenchyma tissue of *Aristolochia macrophylla*. The time-dependence is shown by the variation in the amount of energy dissipation with loading rates. However, they did not provide detailed time-dependent responses, e.g., creep, stress relaxation, etc., which makes it difficult, or impossible, to calibrate the parameters needed for the viscoelastic response (E_N, E_V, μ). As we can see from Eqs. (9) and (10), when $\varepsilon_V^d = 0$, the constitutive relations become:

$$\begin{aligned} \varepsilon_N &= -\frac{\partial G}{\partial \sigma_N} = \frac{\alpha \sigma_N}{E_{Nf}} + \frac{(1-\alpha)\sigma_N}{E_{No}} \\ \varepsilon_V &= -\frac{\partial G}{\partial \sigma_V} = \frac{\alpha \sigma_V}{E_{Vf}} + \frac{(1-\alpha)\sigma_V}{E_{Vo}} \end{aligned} \tag{23}$$

Together with the kinematic condition shown in Eq. (3) and equilibrium condition $\sigma = \sigma_N + \sigma_V$, the reversible strain derived from Eq. (23) can be written as follow:

$$\left(E_N + E_V\right)\varepsilon_e = \sigma \tag{24}$$

where

$$\begin{aligned} \frac{1}{E_V} &= \frac{\alpha}{E_{Vf}} + \frac{(1-\alpha)}{E_{Vo}} \\ \frac{1}{E_N} &= \frac{\alpha}{E_{Nf}} + \frac{(1-\alpha)}{E_{No}} \end{aligned} \tag{25}$$

The calibration of elastic moduli of the original network and newly formed network for time-independent constitutive relation shown in Eq. (24) were discussed in previous section. From Eq. (25), the elastic modulus at the initial state $\left(E_N + E_V\right)|_{\alpha=0} = E_o = E_{No} + E_{Vo}$; at final state, $\left(E_N + E_V\right)|_{\alpha=1} = E_f = E_{Nf} + E_{Vf}$. The values for E_o and E_f are depicted in Table 1. For the

purpose of a qualitative study, we take $E_{No} = E_{Vo} = \frac{1}{2}E_o$ and $E_{Nf} = E_{Vf} = \frac{1}{2}E_f$. For the viscosity parameter μ, we set the characteristic time $\tau = 2000s$, hence we have $\mu_o = \tau E_{Vo}$ and $\mu_f = \tau E_{Vf}$. The above material parameters $E_{No}, E_{Vo}, \mu_o, E_{Nf}, E_{Vf}, \mu_f$ can be easily determined if we have the experimental data reported in time-domain at the initial and final configurations, see previous work of Muliana et al. (2016) and Song et al. (2019).

The relation between the microstructural change α and driving force F for the time-dependent model is assumed to be the same as the one from the time-independent model, which can be determined by examining the outerloop of the time-independent hysteresis loop, as discussed in the previous section.

A qualitative study for the effect of viscoelasticity on the hysteresis behavior is depicted in Figure 6. The loading stress cycles between 0MPa and 80MPa, and energy dissipations per cycle are calculated for different loading rates. The left figure in Figure 6 shows the energy dissipation for the first three cycles. As we can see from the figure, the energy dissipation of the first cycle is significantly larger than the second and third cycles. The reason for a higher energy dissipation for the first cycle is because more pronounced microstructural changes and time-dependent effect occur during first cycle, therefore more energy are dissipated. As reloading continues, the response is closer to the relaxed stage and microstructural changes vary between the reloading-unloading strains (1.8-4.8%), and hence smaller energy dissipation is seen. Thus, it can be seen that there are two sources of energy dissipation, which are from the microstructural changes and the viscous effect. Figure 8 shows time-dependent hysteresis responses of cycles 1-3, respectively, at loading rate $\dot{\sigma} = 1 \times 10^{-2} MPa/s$. As we can see from Figure 7(a), more deformation occurs during first cycle, which leads to more pronounced energy dissipation, as shown in Figure 6(left). From Figure

7(b) and (c), we can see that the shapes of the hysteresis loop for cycle 2 and cycle 3 are almost the same, which means the response reaches the steady-state. The right figure of Figure 6 shows the ratio between the dissipated energy and stored energy for the third cycle. Initially the energy dissipation increases with stress rate, then after reaching a peak, energy dissipation decreases with increasing stress rate. The relation between the energy dissipation and stress rate depicted in Figure 6 shows that the model can capture the same trend as the experimental result reported in Figures 4 and 5 of Köhler and Spatz (2002). The time-dependent model adequately describes the effect of viscoelasticity on the hysteresis response.

A simulation for creep responses using the time-dependent model is depicted in Figure 8. Two stress levels, 40MPa (left) and 80MPa (right), are considered in this analysis. The loading stress is held for 1 hour. From Figure 8, we can see that the time-dependent model is capable of generating a creep-recovery curve similar to a typical linear viscoelastic material. However, unlike a linear viscoelastic material, the instantaneous deformations shown in Figure 8 during loading and unloading are not the same. The difference in the instantaneous deformations is attributed to the continuous microstructural changes during creep. Comparing the left figure of Figure 9 to the right figure, we can see that the difference in the instantaneous deformations during loading and unloading is more obvious for the larger stress, indicating more microstructural changes occur at 80MPa. Figure 8 clearly presents the two sources of an energy dissipation: the dissipation due to a microstructural change and the dissipation due to a viscoelastic effect.

Predicting Nonlinear Hysteretic Responses of Plant Stems

Plant stems are composites comprised of multiple constituents with different microstructural morphologies. In a simplistic way, they can be considered as composites having outer

strengthening tissue and inner core. The outer strengthening tissue consists of collenchyma, parenchyma, and sclerenchyma while the inner core comprises of phloem, xylem bundles, interfascicular parenchyma and pith (Köhler and Spatz 2002). We can predict the overall response of composites by incorporating different responses of the constituents and amount of the constituents in the composites, i.e., using a micromechanics model. We assume the stems as composites comprising of two different constituents (Figure 9), i.e., outer strengthening tissue and inner core, as tested by Köhler and Spatz (2002).

Similar to the simulation of individual plant tissues discussed above, we assume both the outer ring and inner core experience different microstructural changes when subjected to external stimuli. For a composite with two constituents, the Gibbs potential of the stem is written as:

$$G(c,\alpha_1,\alpha_2,\sigma_1,\sigma_2)=(1-c)\left[-\left(\frac{\alpha_1\sigma_1^{\,2}}{2E_{1f}}+\frac{(1-\alpha_1)\sigma_1^{\,2}}{2E_{1o}}\right)\right]+c\left[-\left(\frac{\alpha_2\sigma_2^{\,2}}{2E_{2f}}+\frac{(1-\alpha_2)\sigma_2^{\,2}}{2E_{2o}}\right)\right] \quad (26)$$

where

c: Volume fraction of the inner core tissue

σ_1,σ_2: Independent variables represent stresses applied on the outer skin and inner core, respectively.

E_{1o},E_{1f}: Moduli of the outer strengthening tissue at $\alpha_1=0$ (initial state) and $\alpha_1=1$ (complete microstructural change), respectively.

E_{2in},E_{2f}: Moduli of the inner core tissue at $\alpha_2=0$ and $\alpha_2=1$, respectively.

Following Eq. (20), the rate of energy dissipation for the stem is written as:

$$\xi=(1-c)\sigma_1\left(\dot{\varepsilon}_1-\dot{\varepsilon}_{1e}\right)+c\sigma_2\left(\dot{\varepsilon}_2-\dot{\varepsilon}_{2e}\right)-\frac{\partial G}{\partial\alpha_1}\dot{\alpha}_1-\frac{\partial G}{\partial\alpha_2}\dot{\alpha}_2 \quad (27)$$

The elastic strains for the outer skin and inner core tissues are:

$$\begin{aligned}(1-c)\varepsilon_{1e} &= -\frac{\partial G}{\partial \sigma_1} = (1-c)\left[\frac{\alpha_1\sigma_1}{E_{1f}} + \frac{(1-\alpha_1)\sigma_1}{E_{1o}}\right] \\ c\varepsilon_{2e} &= -\frac{\partial G}{\partial \sigma_2} = c\left[\frac{\alpha_2\sigma_2}{E_{2f}} + \frac{(1-\alpha_2)\sigma_2}{E_{2o}}\right]\end{aligned} \tag{28}$$

and we also assumed that

$$\begin{aligned}\varepsilon_1 - \varepsilon_{1e} = \alpha_1\varepsilon_{1\max} &\rightarrow \dot{\varepsilon}_1 - \dot{\varepsilon}_{1e} = \dot{\alpha}_1\varepsilon_{1\max} \\ \varepsilon_2 - \varepsilon_{2e} = \alpha_2\varepsilon_{2\max} &\rightarrow \dot{\varepsilon}_2 - \dot{\varepsilon}_{2e} = \dot{\alpha}_2\varepsilon_{2\max}\end{aligned} \tag{29}$$

From Eqs. (28) and (29), the strains for the outer strengthening skin and inner core are:

$$\begin{aligned}\varepsilon_1 &= \alpha_1\varepsilon_{1\max} + \left[\frac{\alpha_1\sigma_1}{E_{1f}} + \frac{(1-\alpha_1)\sigma_1}{E_{1o}}\right] \\ \varepsilon_2 &= \alpha_2\varepsilon_{2\max} + \left[\frac{\alpha_2\sigma_2}{E_{2f}} + \frac{(1-\alpha_2)\sigma_2}{E_{2o}}\right]\end{aligned} \tag{30}$$

Substituting Eqs. (28) and (29) into Eq. (27), the rate of energy dissipation for the stem is:

$$\xi = \left[(1-c)\sigma_1\varepsilon_{1\max} - \frac{\partial G}{\partial \alpha_1}\right]\dot{\alpha}_1 + \left(c\sigma_2\varepsilon_{2\max} - \frac{\partial G}{\partial \alpha_2}\right)\dot{\alpha}_2 = (1-c)F_1\dot{\alpha}_1 + cF_2\dot{\alpha}_2 \tag{31}$$

where F_1 and F_2 are the driving forces for microstructural changes of the outer skin tissue and inner core tissue, respectively, which are:

$$\begin{aligned}F_1 &= \sigma_1\varepsilon_{1\max} + \sigma_1^{\,2}\left(\frac{1}{2E_{1f}} - \frac{1}{2E_{1o}}\right) \\ F_2 &= \sigma_2\varepsilon_{2\max} + \sigma_2^{\,2}\left(\frac{1}{2E_{2f}} - \frac{1}{2E_{2o}}\right)\end{aligned} \tag{32}$$

The microstructural changes of the outer skin and inner core are:

$$\alpha_1 = \frac{\varepsilon_1 - \dfrac{\sigma_1}{E_{1o}}}{\dfrac{\sigma_1}{E_{1f}} - \dfrac{\sigma_1}{E_{1o}} + \varepsilon_{1max}}; \qquad \alpha_2 = \frac{\varepsilon_2 - \dfrac{\sigma_2}{E_{2o}}}{\dfrac{\sigma_2}{E_{2f}} - \dfrac{\sigma_2}{E_{2o}} + \varepsilon_{2max}} \tag{33}$$

For stems with a structure shown in Figure 9, the following kinematic and equilibrium equations for the axial loading are considered:

$$\begin{aligned} \varepsilon_1 &= \varepsilon_2 = \varepsilon \\ \sigma &= (1-c)\sigma_1 + c\sigma_2 \end{aligned} \tag{34}$$

From Eqs. (30) and (34) the constitutive equation for the stalk is:

$$\left[\frac{(1-c)}{\frac{\alpha_1}{E_{1f}} + \frac{1-\alpha_1}{E_{1o}}} + \frac{c}{\frac{\alpha_2}{E_{2f}} + \frac{1-\alpha_2}{E_{2o}}} \right] \varepsilon = \sigma + \frac{\alpha_1 (1-c)\varepsilon_{1\max}}{\frac{\alpha_1}{E_{1f}} + \frac{1-\alpha_1}{E_{1o}}} + \frac{\alpha_2 c \varepsilon_{2\max}}{\frac{\alpha_2}{E_{2f}} + \frac{1-\alpha_2}{E_{2o}}} \tag{35}$$

Figure 11 shows the stress-strain behaviors of the outer strengthening and inner core tissues of *Aristolochia macrophylla* stem. The experimental data are obtained from Köhler and Spatz (2002). For each of the outer and inner core tissues, material parameters are determined from the stress-strain in Figure 10. The corresponding driving force and microstructural changes for the outer strengthening and inner core tissues are obtained from Eqs. (32) and (33), as depicted in Figure 11. The material parameters are listed in Table 1. Figure 12 presents a prediction of a nonlinear response of *Aristolochia macrophylla* stem. The volume fraction of the inner core is determined by varying its value to give the best result of the overall response of the stem. In this study, the volume fraction of 0.6 is chosen. Figure 13 shows the simulation of cyclic response for *Aristolochia macrophylla* stem, where input stress is varied between 0 MPa and 16 MPa. For comparison, the hysteretic responses of the outer skins and inner core are also shown.

Conclusions

We have modeled a nonlinear hysteretic response of plant tissues and stems subjected to cyclic mechanical loadings. We formulated a constitutive model, based on thermodynamics and continuum mechanics, by taking into account the net effect of microstructural changes in

describing the macroscopic response of the cell wall. The model treats the cell wall as a homogenized medium, and the effect of microstructural changes is incorporated through an internal state variable. A typical experimental test in understanding the biomechanics of plants is obtained by testing tissues at a relatively large scale, which are inherently treating the plant tissues as homogenized bodies. The proposed model correlates well with the typical experimental tests since the detailed processes or information of the microstructural aspects that influence the macroscopic response of plant tissues are often not available, and only the net effect is being accounted for. The model assumed that prescribing a mechanical loading to plant tissues alter the microstructures of tissues from the initial configuration (original network) to the final configuration (complete changes of microstructures, or new network). At these two extreme configurations, the plant tissues have different mechanical and physical properties associated with the two networks. At any intermediate loading stage, the macroscopic response of the plant tissues is due to a combined effect of the initial and final microstructures. The model also accounts for an energy dissipation, which are due to the viscoelastic effect and microstructural changes. We have compared the responses obtained from the proposed model to several available nonlinear hysteretic responses of plant tissues. Overall, the model shows a good correlation with experimental data. One of the advantages of the model is that it has relatively small numbers of material parameters that can be easily calibrated from the macroscopic experimental data. The material parameters have physical interpretation instead of mainly for curve fitting purposes. The model also incorporates gradual microstructural changes during various loading histories.

We have also demonstrated that the proposed approach can be extended easily to include responses of different tissues in the plant stem in predicting the overall mechanical response of the stem. This will be useful for examining the contributions of different constituents in the plant stem

on their macroscopic mechanical response, which can shed light into understanding deformation mechanisms in plant stem.

Acknowledgement

This research is sponsored by the National Science Foundation under grant CMMI 1761015.

References

Altaner, C. and M. Jarvis (2008). *Modelling polymer interactions of the 'molecular Velcro'type in wood under mechanical stress*. **253**(3): 434-445.

Borodulina, S., A. Kulachenko and D. Tjahjanto (2015). *Constitutive modeling of a paper fiber in cyclic loading applications*. Computational Materials Science **110**: 227-240.

Brulé, V., A. Rafsanjani, D. Pasini and T. L. Western (2016). *Hierarchies of plant stiffness*. Plant Science **250**: 79-96.

Burgert, I. (2006). *Exploring the micromechanical design of plant cell walls*. American journal of botany **93**(10): 1391-1401.

De Tommasi D, Puglisi G, and Saccomandi G (2006), "A Micromechanics-based Model for the Mullins Effect" J. Rheology, 50, pp. 495-512

De Tommasi D, Puglisi G, Saccomandi G. (2010), "Damage, self-healing, and hysteresis in spider silks," Biophys. J. 98, 1941–1948

Doraiswamy, S., A. Rao and A. Srinivasa (2011). *Combining thermodynamic principles with preisach models for superelastic shape memory alloy wires*. Smart Materials and Structures **20**(8): 085032.

Fratzl, P., H. Gupta, E. Paschalis and P. Roschger (2004). *Structure and mechanical quality of the collagen–mineral nano-composite in bone*. Journal of materials chemistry **14**(14): 2115-2123.

Gibson, L. J. (2012). *The hierarchical structure and mechanics of plant materials*. Journal of the Royal Society Interface: rsif20120341.

Gomez, F. E., A. H. Muliana, K. J. Niklas and W. L. Rooney (2017). *Identifying Morphological and Mechanical Traits Associated with Stem Lodging in Bioenergy Sorghum (Sorghum bicolor)*. BioEnergy Research **10**(3): 635-647.

Hayot, C. M., E. Forouzesh, A. Goel, Z. Avramova and J. A. Turner (2012). *Viscoelastic properties of cell walls of single living plant cells determined by dynamic nanoindentation*. Journal of experimental botany **63**(7): 2525-2540.

Hogan, C. J. and K. J. Niklas (2004). *Temperature and water content effects on the viscoelastic behavior of Tilia americana (Tiliaceae) sapwood*. Trees **18**(3): 339-345.

Köhler, L. and H.-C. Spatz (2002). *Micromechanics of plant tissues beyond the linear-elastic range*. Planta **215**(1): 33-40.

Lee S, Zargar O, Gomez F, Pharr M, Muliana A, Finlayson SA (2019), "Time-dependent Mechanical Behavior of Sorghum Bicolor Stems" under review

Lichtenegger, H., A. Reiterer, S. Stanzl-Tschegg and P. Fratzl (1999). *Variation of cellulose microfibril angles in softwoods and hardwoods—a possible strategy of mechanical optimization*. Journal of structural biology **128**(3): 257-269.

Lindström, H., J. W. Evans and S. P. Verrill (1998). *Influence of cambial age and growth conditions on microfibril angle in young Norway spruce (Picea abies [L.] Karst.)*. Holzforschung-International Journal of the Biology, Chemistry, Physics and Technology of Wood **52**(6): 573-581.

Mayergoyz, I. (1986). *Mathematical models of hysteresis*. IEEE Transactions on magnetics **22**(5): 603-608.

Mayergoyz, I. D. (2003). *Mathematical models of hysteresis and their applications*, Academic Press.

Muliana, A., K. Rajagopal, D. Tscharnuter and G. Pinter (2016). *A nonlinear viscoelastic constitutive model for polymeric solids based on multiple natural configuration theory*. International Journal of Solids and Structures **100**: 95-110.

Navi, P., P. K. Rastogi, V. Gresse and A. Tolou (1995). *Micromechanics of wood subjected to axial tension*. Wood Science and Technology **29**(6): 411-429.

Navi, P. and M. Sedighi-Gilani (2004). *Modeling the influences of microfibril angles and natural defects on the force-extension behavior of single wood fibers*. COST E20 book: 57-70.

Niklas, K. J. (1992). *Plant biomechanics: an engineering approach to plant form and function*, University of Chicago press.

Park, Y. B. and D. J. Cosgrove (2012). *Changes in cell wall biomechanical properties in the xyloglucan-deficient xxt1/xxt2 mutant of Arabidopsis*. Plant physiology **158**(1): 465-475.

Rajagopal, K. and A. Srinivasa (2004). *On the thermomechanics of materials that have multiple natural configurations. Part II: Twinning and solid to solid phase transformation*. Zeitschrift für angewandte Mathematik und Physik **55**(6): 1074-1093.

Rajagopal, K. R. and L. Tao (1995). *Mechanics of mixtures*, World scientific.

Rajagopal, K. R. and A. S. Wineman (1992). *A constitutive equation for nonlinear solids which undergo deformation induced microstructural changes*. International Journal of Plasticity **8**(4): 385-395.

Robertson, D. J., M. Julias, S. Y. Lee and D. D. Cook (2017). *Maize stalk lodging: morphological determinants of stalk strength*. Crop Science **57**(2): 926-934.

Robertson, D. J., S. Y. Lee, M. Julias and D. D. Cook (2016). *Maize stalk lodging: Flexural stiffness predicts strength*. Crop Science **56**(4): 1711-1718.

Salmen, L. (1984). *Viscoelastic properties ofin situ lignin under water-saturated conditions*. Journal of Materials Science **19**(9): 3090-3096.

Shah, D. U., T. P. Reynolds and M. H. Ramage (2017). *The strength of plants: theory and experimental methods to measure the mechanical properties of stems*. Journal of experimental botany **68**(16): 4497-4516.

Singh, F., Katiyar, V. K., & Singh, B. P. (2013). *A new strain energy function to characterize apple and potato tissues*. Journal of food engineering, 118(2), 178-187

Song, R., H. B. Atitallah, A. H. Muliana and Z. Ounaies (2018). *Hysteretic electro-mechanical coupling response of PZT fibers: Constitutive modeling and experiments*. Ferroelectrics **526**(1): 95-119.

Song R, Muliana A, and Rajagopal KR (2019), *A thermodynamically consistent model for viscoelastic polymers undergoing microstructural changes*, International J. Engineering Science, 142, pp. 106-124

Spatz, H., L. Kohler and K. Niklas (1999). *Mechanical behaviour of plant tissues: composite materials or structures?* Journal of Experimental Biology **202**(23): 3269-3272.

Speck, O., and Spatz, H. C. (2003). Mechanical properties of the rhizome of Arundo donax L. *Plant Biology*, *5*(06), 661-669

Speck, T. and I. Burgert (2011). *Plant stems: functional design and mechanics*. Annual Review of Materials Research **41**: 169-193.

Trivaudey, F., Placet, V., Guicheret-Retel, V., & Boubakar, M. L. (2015). *Nonlinear tensile behaviour of elementary hemp fibres. Part II: Modelling using an anisotropic viscoelastic constitutive law in a material rotating frame*. Composites Part A: Applied Science and Manufacturing, 68, 346-355

Xing, J., M. Radovic and A. Muliana (2017). *A nonlinear constitutive model for describing cyclic mechanical responses of BaTiO3/Ag composites*. Acta Mechanica **228**(6).

Yuan, Z., A. Muliana and K. Rajagopal (2017). *Quasi-linear viscoelastic modeling of light-activated shape memory polymers*. Journal of Intelligent Material Systems and Structures **28**(18): 2500-2515.

Zhu, H. X., & Melrose, J. R. (2003). *A mechanics model for the compression of plant and vegetative tissues*. Journal of theoretical biology, 221(1), 89-101

Table 1 Material Parameters for different tissue

Tissue type	E_o (GPa)	E_f (GPa)	ε_{max} (%)	N
Wet wood tissue of spruce (*Picea abies*)	1.189	1.757	13.65	5050
Isolated sclerenchyma tissue of *Aristolochia macrophylla*	3.542	4.984	4.24	5050
Outer strengthening tissue of *Aristolochia macrophylla*	1.552	1.552	2.91	5050
Inner core tissue of *Aristolochia macrophylla*	0.262	0.262	8.37	5050

Figures:

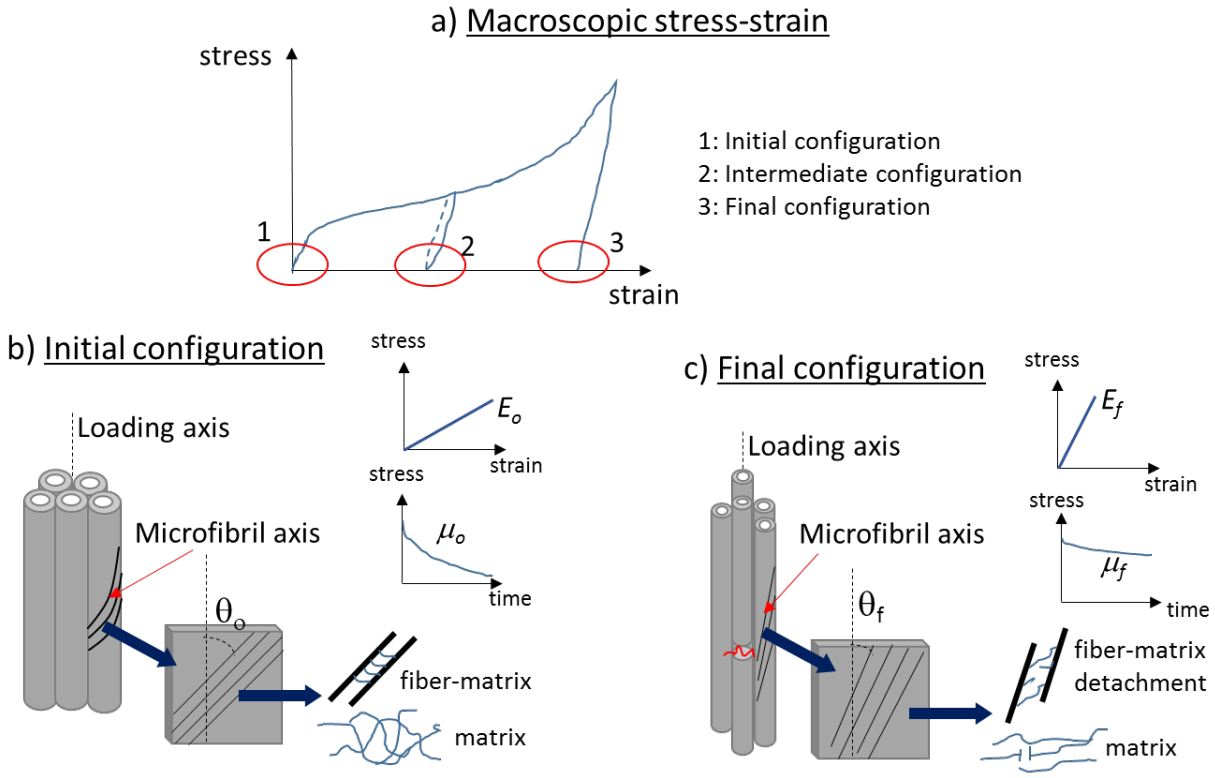

Figure 1 A schematic representation of a nonlinear hysteretic response and the motivation of microstructural changes

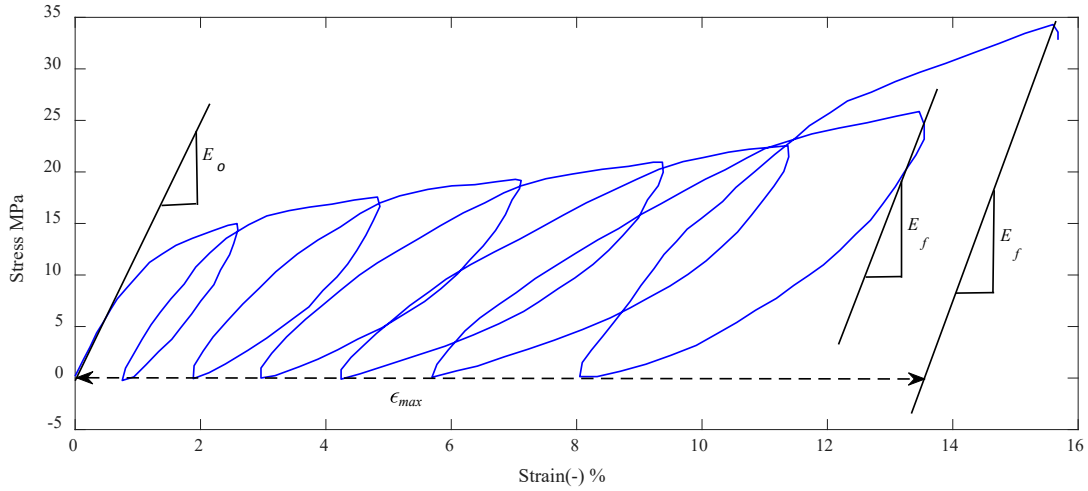

Figure 2 Calibration of material parameters E_o, E_f and $\varepsilon_{\max}$ from experimental data on wet wood tissue of spruce (Burgert 2006)

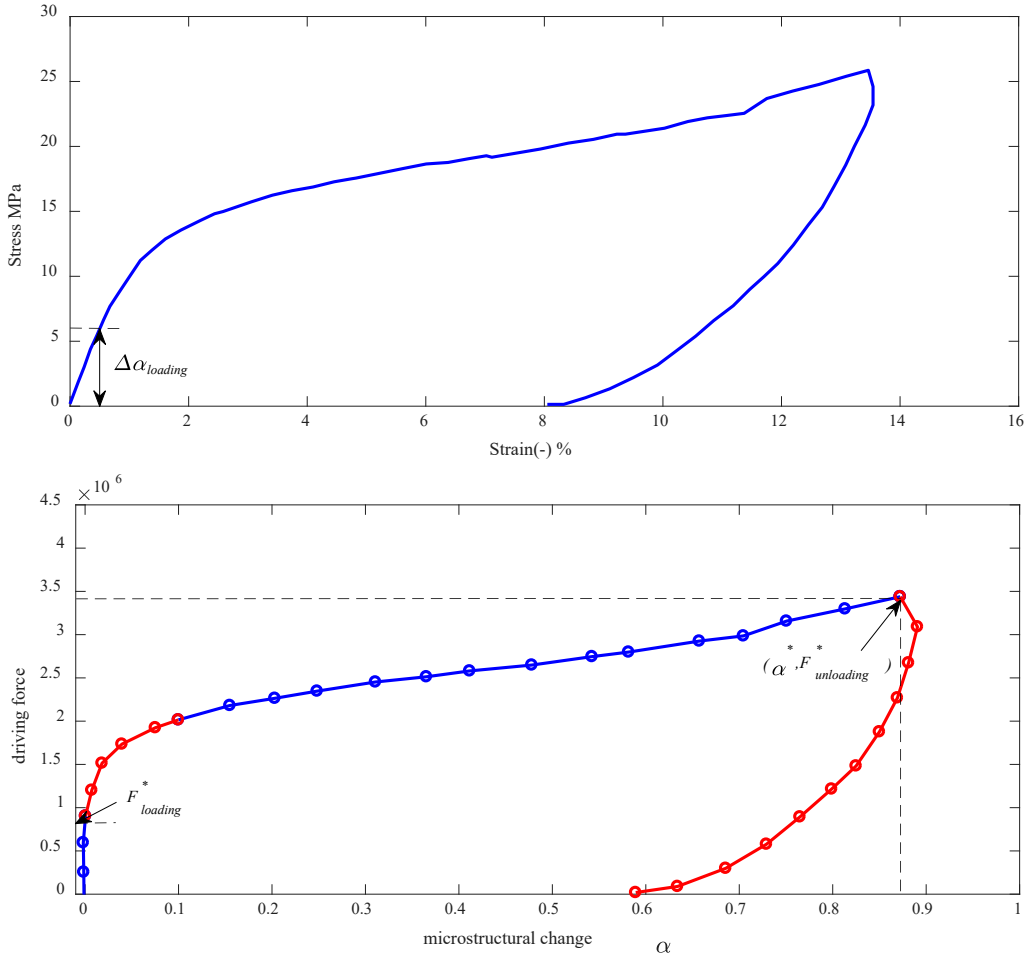

Figure 3 Outer loop of the hysteretic response (top) and its corresponding driving force and microstructural changes (bottom)

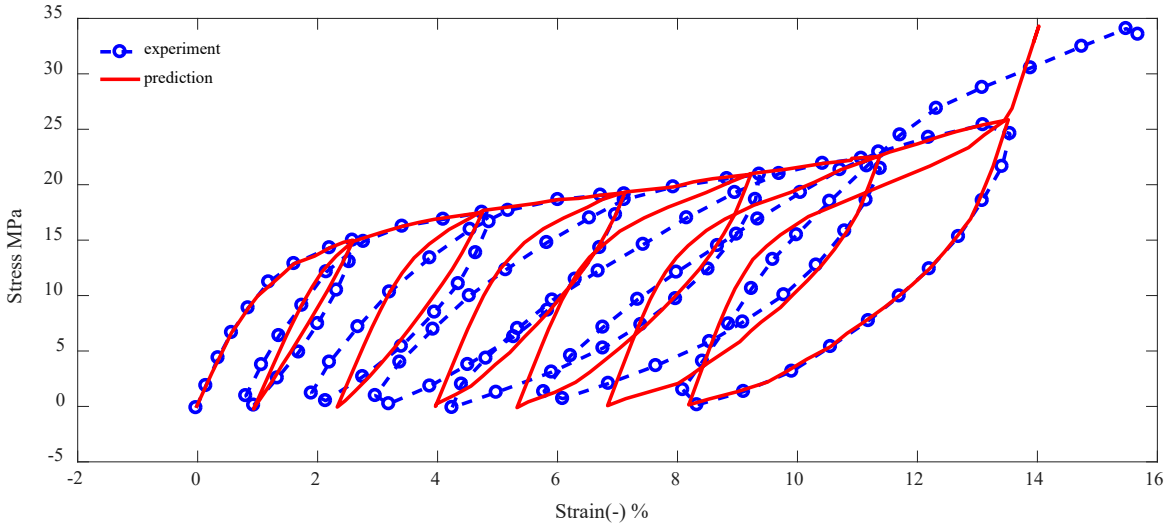

Figure 4 Modeling result of wet wood tissue of spruce

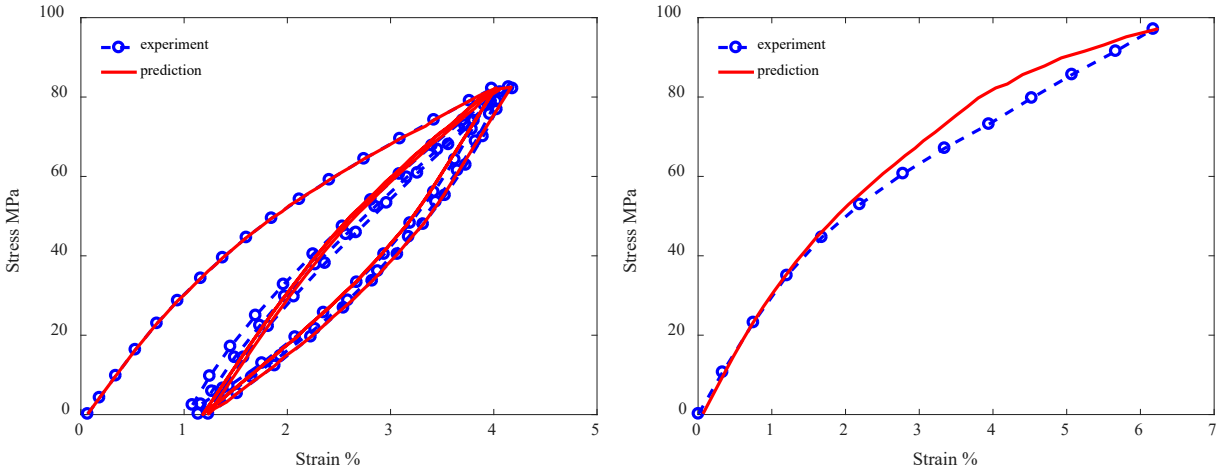

Figure 5 Simulation results for isolated sclerenchyma tissue of *Aristolochia macrophylla. Left: cyclic response. Right: Quasi static response.*

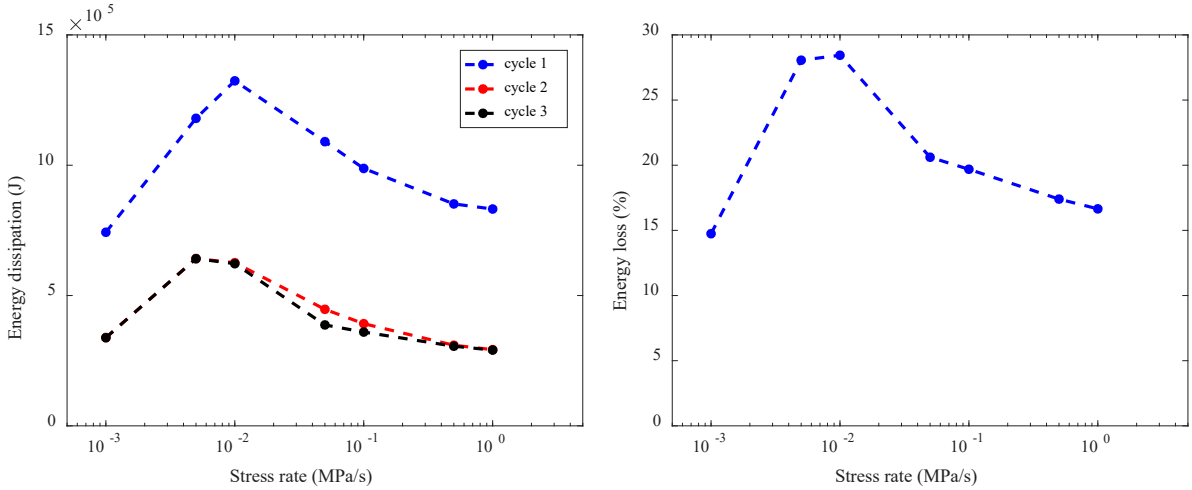

Figure 6 Quantitative study for the effect of viscoelasticity on hysteresis behavior

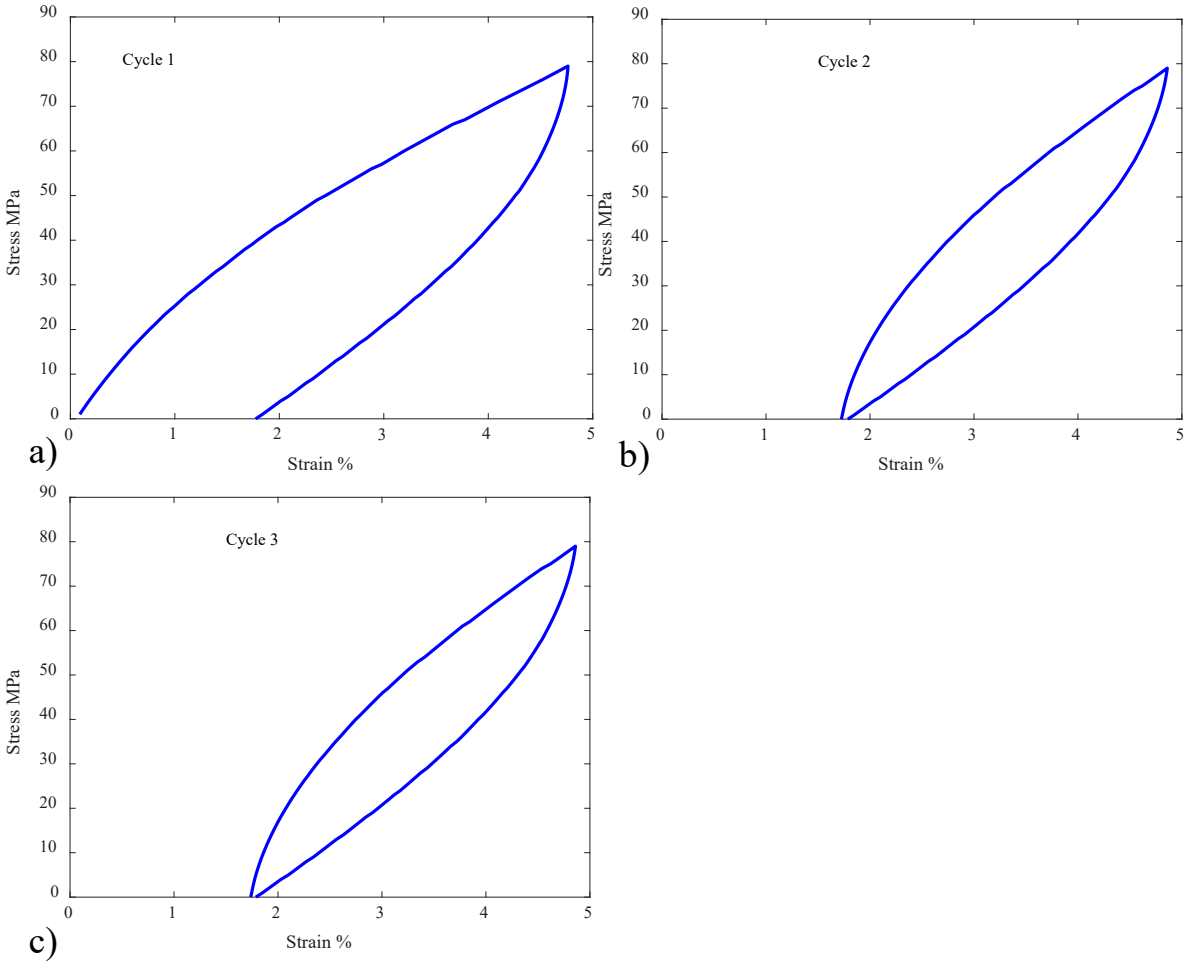

Figure 7 Time-dependent hysteresis response at stress rate $\dot{\sigma} = 1 \times 10^{-2}\, MPa / s$

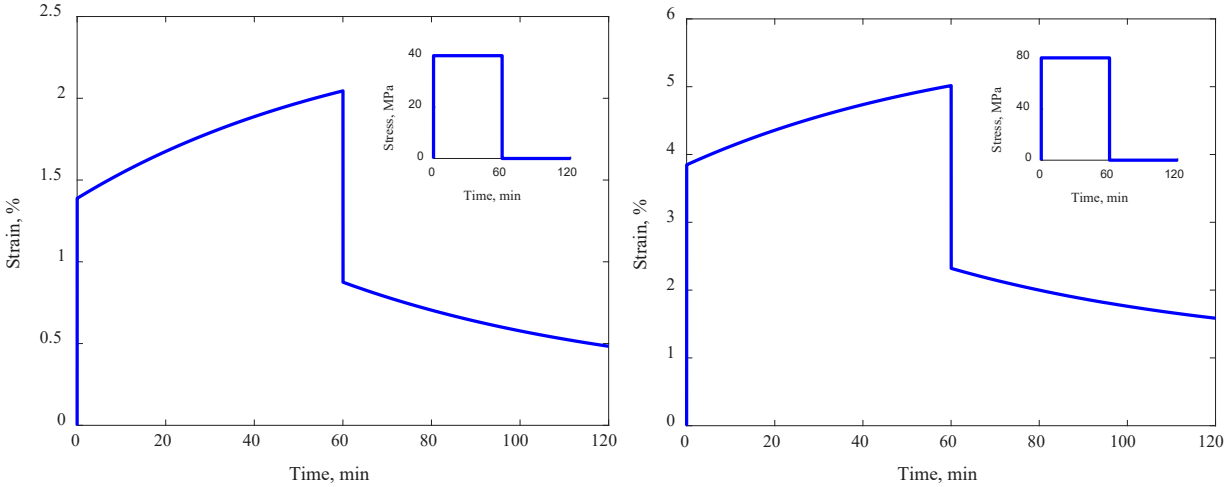

Figure 8 Creep responses generated by time-dependent model

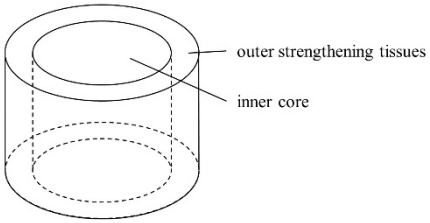

Figure 9 Structure of plant tissue (stalk)

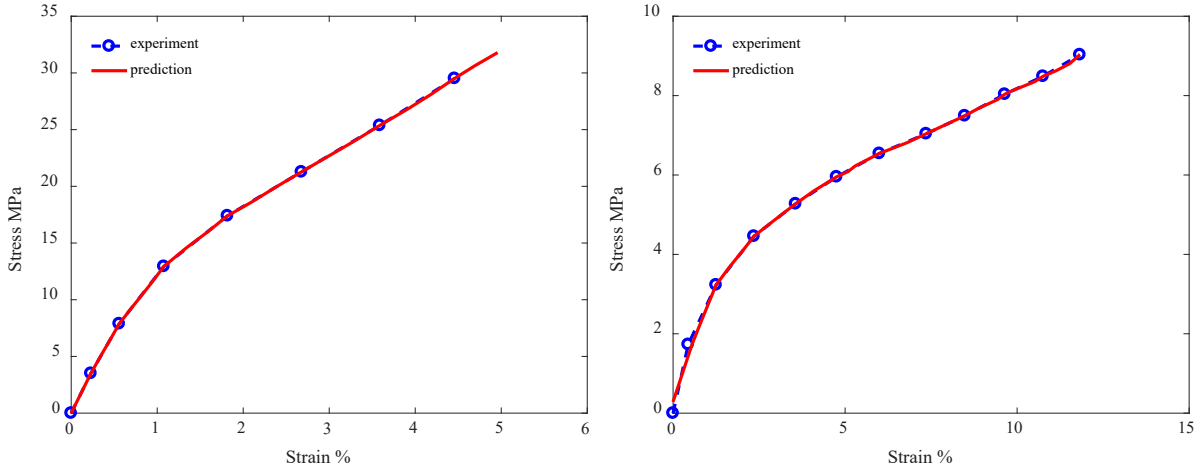

Figure 10 Simulation of strain-stress responses for outer skin and inner core of the *Aristolochia macrophylla* stem. Left: simulation for outer skin tissue. Right: simulation for inner core. Experimental data are obtained from Köhler and Spatz (2002)

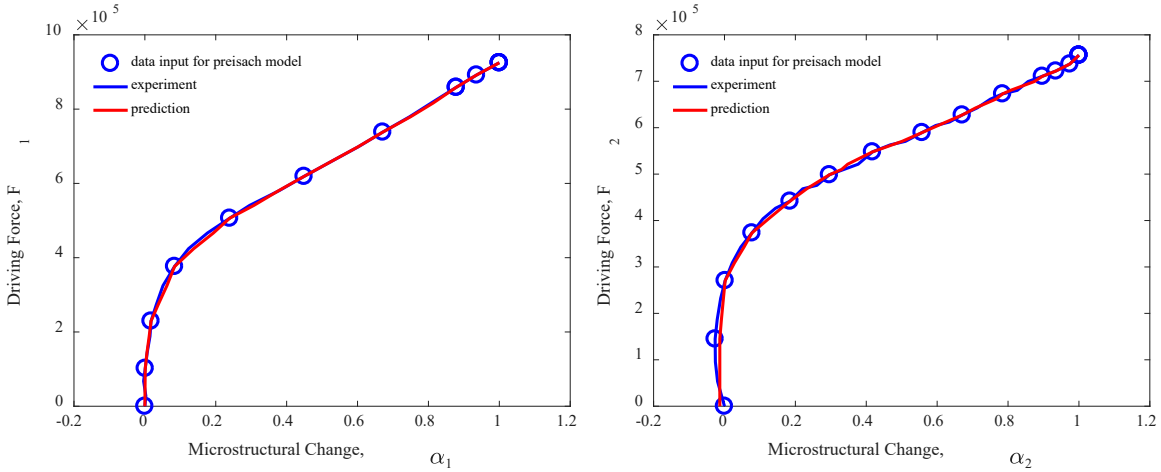

Figure 11 Relation between driving force and microstructural change for *Aristolochia macrophylla* tissue

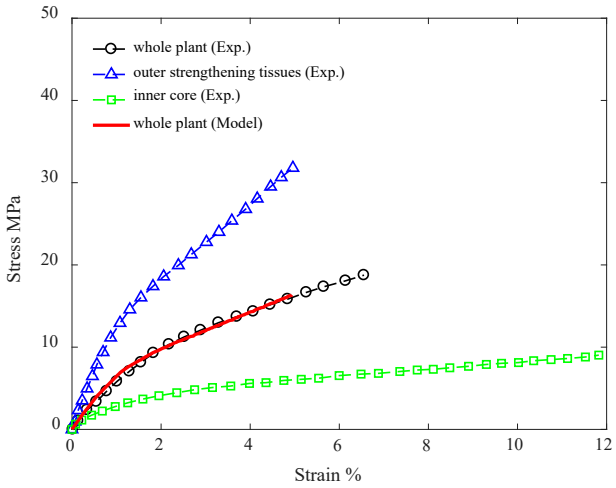

Figure 12 Response of the *Aristolochia macrophylla* stem with inner core volume fraction of 0.6

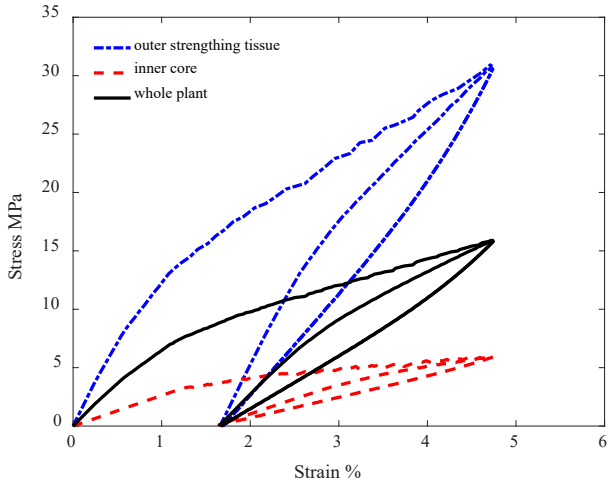

Figure 13 Simulation for the cyclic response of *Aristolochia macrophylla* stem

Appendix A

A general multi-axial constitutive model that can be used for describing anisotropic response of materials is discussed here. To calibrate the properties in the multi-axial model, experimental tests beyond a simple uniaxial test are required. The Gibbs free energy is expressed in terms of stress tensor comprising elastic (N) and viscoelastic (V) components, $G = G(\boldsymbol{\sigma}_V, \boldsymbol{\sigma}_N, \alpha)$ and the total strain tensor is given as:

$$\boldsymbol{\varepsilon} = \boldsymbol{\varepsilon}_e + \boldsymbol{\varepsilon}_p \tag{A.1}$$

where $\boldsymbol{\varepsilon}_e = \boldsymbol{\varepsilon}_V = \boldsymbol{\varepsilon}_N$, $\boldsymbol{\varepsilon}_V = \boldsymbol{\varepsilon}_V^e + \boldsymbol{\varepsilon}_V^v$ and $\boldsymbol{\varepsilon}_p$ is the permanent strain tensor. The elastic strains are determined from $\boldsymbol{\varepsilon}_N = -\dfrac{\partial G}{\partial \boldsymbol{\sigma}_N}$ and $\boldsymbol{\varepsilon}_V^e = -\dfrac{\partial G}{\partial \boldsymbol{\sigma}_V}$. The total stress is $\boldsymbol{\sigma} = \boldsymbol{\sigma}_N + \boldsymbol{\sigma}_V$. The rate of the mechanical dissipation is given as:

$$\xi = \boldsymbol{\sigma}_V \dot{\boldsymbol{\varepsilon}}_V^d + \boldsymbol{\sigma}\dot{\boldsymbol{\varepsilon}}_p - \frac{\partial G}{\partial \alpha}\dot{\alpha} = \xi_D + \left(\boldsymbol{\sigma}\frac{\partial \boldsymbol{\varepsilon}_P}{\partial \alpha} - \frac{\partial G}{\partial \alpha}\right)\dot{\alpha} = \xi_D + F_\alpha \dot{\alpha} \tag{A.2}$$

For a general multi-axial response, the Gibbs free energy can be expressed as:

$$G(\boldsymbol{\sigma}_V, \boldsymbol{\sigma}_N, \alpha) = -\left[\alpha \mathbf{S}_V^f \boldsymbol{\sigma}_V . \boldsymbol{\sigma}_V + (1-\alpha)\mathbf{S}_V^i \boldsymbol{\sigma}_V . \boldsymbol{\sigma}_V\right] - \left[\alpha \mathbf{S}_N^f \boldsymbol{\sigma}_N . \boldsymbol{\sigma}_N + (1-\alpha)\mathbf{S}_N^i \boldsymbol{\sigma}_N . \boldsymbol{\sigma}_N\right] \tag{A.3}$$

where $\mathbf{S}_V^f, \mathbf{S}_V^i, \mathbf{S}_N^f, \mathbf{S}_N^i$ are fourth order tensors associated with the compliance of the materials. The components of the above tensors should be determined from experiments, which will indicate the isotropy or anisotropy nature of the materials. The rate of the mechanical dissipation associated with the delayed response is given as:

$$\xi_D = \alpha \mathbf{K}^f \boldsymbol{\sigma}_V . \boldsymbol{\sigma}_V + (1-\alpha)\mathbf{K}^i \boldsymbol{\sigma}_V . \boldsymbol{\sigma}_V \tag{A.4}$$

where $\mathbf{K}^f$ and $\mathbf{K}^i$ are fourth order tensors associated with the inverse viscosity of the materials.

Finally, the elastic and viscoelastic strain tensors can be determined from the Gibbs energy in Eq. (A.3) and the rate of the dissipative strain can be obtained from Eq. (A.4):

$$\boldsymbol{\varepsilon}_V = \alpha 2\mathbf{S}_V^f \boldsymbol{\sigma}_V + (1-\alpha)2\mathbf{S}_V^i \boldsymbol{\sigma}_V \tag{A.5}$$

$$\boldsymbol{\varepsilon}_N = \alpha 2\mathbf{S}_N^f \boldsymbol{\sigma}_N + (1-\alpha)2\mathbf{S}_N^i \boldsymbol{\sigma}_N \tag{A.6}$$

$$\dot{\boldsymbol{\varepsilon}}_V^d = \alpha 2\mathbf{K}^f \boldsymbol{\sigma}_V + (1-\alpha)2\mathbf{K}^i \boldsymbol{\sigma}_V \tag{A.7}$$

The driving force for the microstructural changes is now given as:

$$F_\alpha = \boldsymbol{\sigma}\frac{\partial \boldsymbol{\varepsilon}_p}{\partial \alpha} + \mathbf{S}_V^f \boldsymbol{\sigma}_V . \boldsymbol{\sigma}_V - \mathbf{S}_V^i \boldsymbol{\sigma}_V . \boldsymbol{\sigma}_V + \mathbf{S}_N^f \boldsymbol{\sigma}_N . \boldsymbol{\sigma}_N - \mathbf{S}_N^i \boldsymbol{\sigma}_N . \boldsymbol{\sigma}_N \tag{A.8}$$

The function for $\boldsymbol{\varepsilon}_p(\alpha)$ can be formed based on available experimental data, as discussed above. An example of a multi-axial response for isotropic polymers, obtained from the proposed approach, can be found in Song et al. (2019).

Appendix B

The parametric study for the parameter N is shown in this section. Fig. B1 below depicts the Preisach-Krasnoselskii operator used in this study, where $F_{forward}$ and $F_{backward}$ are the two thresholds for the driving force (Doraiswamy et al. (2011); Xing et al. (2017)). Fig. B1 (left) shows a hysteron element used in the Preisach model, where $F^i_{forward}$ and $F^i_{backward}$ indicate the thresholds for i^{th} hysteron. During loading, when the driving force $F > F^i_{forward}$, the hysteron switches 'on' and gives an output of $\Delta\alpha$. Similarly, during unloading, when the driving force $F < F^i_{backward}$, the hysteron is switched 'off'. In the right figure, each cross mark represents a hysteron element; the shadowed area indicates the hysterons triggered on under current loading history. The total number of hysteron can be related to the hysteron on each side N_{side} through $N = \frac{1}{2} N_{side} \times (N_{side} + 1)$.

Figure B1 Basic hysteron element (left); Preisach-Krasnoselskii operator (right).

In the parametric study shown in Fig. B2 below, we choose $N_{side} = 20, 50, 100, 200$, respectively. From Fig. B2, we can see that the value of N does not influence the shape of the hysteresis loop. Parameter N only has an influence on the smoothness of the simulation result. Larger value for N would decrease zigzags, therefore increase the smoothness of the prediction. However, increasing

the value for *N* would also require more computation time. As show in Fig. B2 the responses with N=5050 and N=20100 do not show a significant variation. In the modeling of spruce tissue, the value for *N* is set to be 5050.

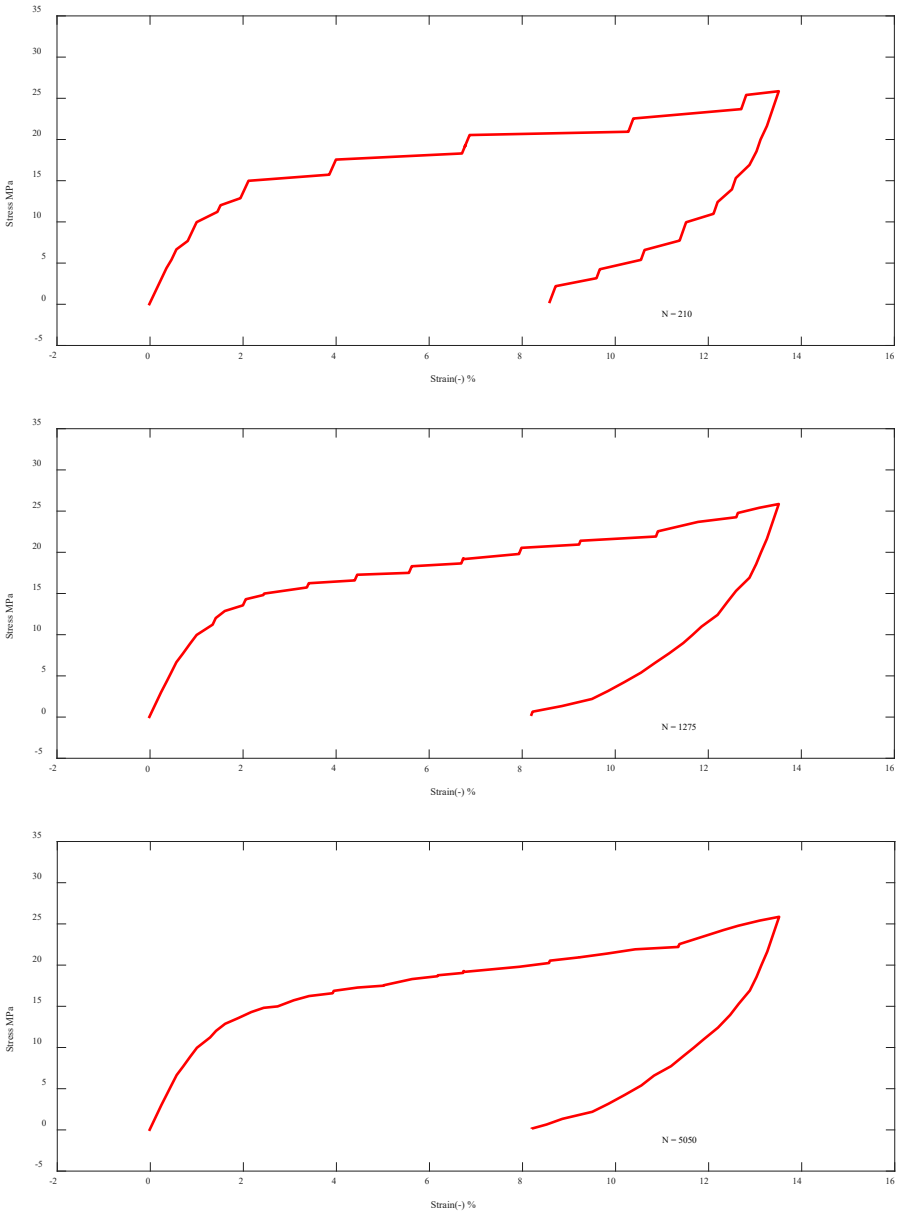

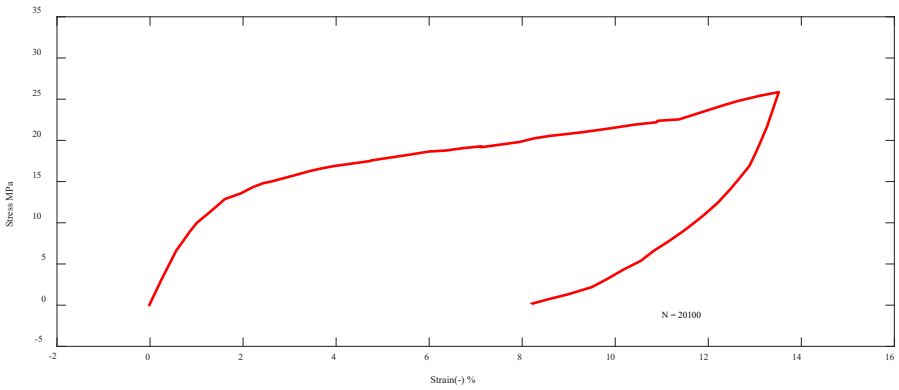

Figure B2 Parametric study for parameter *N*

Appendix C

Besides using the Preisach-Krasnoselskii operator, the relation between driving force F and microstructural change α can also be simulated by picking suitable mathematical functions. The $F-\alpha$ plot calibrated form the outerloop of the hysteresis response can be divided into the following regions:

1. Elastic region.

During loading, if the increase of input stress is smaller than a certain value (as shown in Figure 3 (top)), no microstructural change happens and volume fraction α stays unchanged. In this case, if the increase of loading stress $\Delta\sigma_{loading} \le 6MPa$, we assume no microstructural change occurs.

2. As shown in Figure 3 (bottom), for loading, after elastic region where α stays unchanged, the relation between F and α can be simulated by a second-order polynomial function until they reached a point where α changes linearly with driving force F. For unloading, a second-order polynomial function is enough to describe the relation between F and α. The parts where relations between F and α are modeled by second-order polynomial functions are marked in blue in Figure C1. Eq. (C1) and Eq. (C2) below show the second-order polynomial relations between F and α during the loading and unloading, respectively.

$$\alpha = k_1(F - F^*_{loading})^2 \tag{C1}$$

$$\alpha = \alpha^* - k_2(F - F^*_{unloading})^2 \tag{C2}$$

The value for parameters $F^*_{loading}$, $F^*_{unloading}$ and α^* are marked in Figure 3 (bottom). Values for k_1 and k_2 are calibrated by fitting Eqs. (C1) and (C2) with outerloop of the $F-\alpha$ plot. In this case, the value for k_1 is 7.0×10^{-14}, and the value for k_2 is 2.8×10^{-14}.

3. Linear relation between F and α during loading

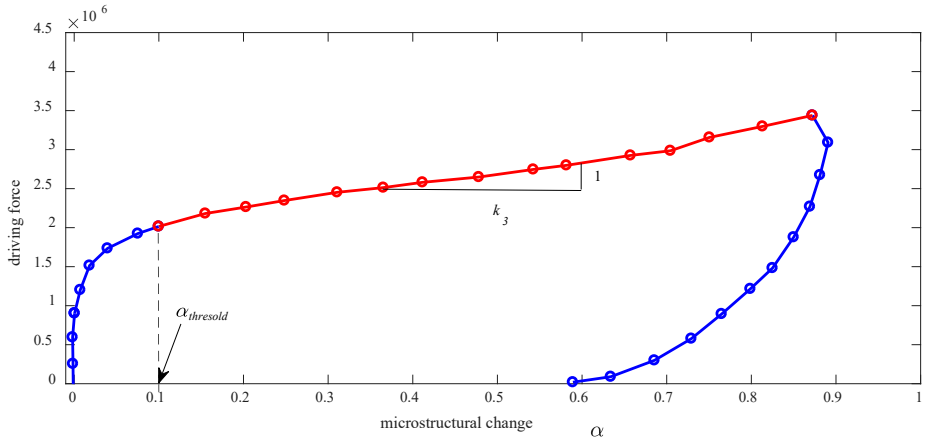

Figure C1 Linear relation between F and α during loading

The red line shown in Fig.B1 is the part where α increase linearly with F. As shown in Fig.B1, it is assumed that when volume fraction α reached a certain value, $\alpha_{threshold}$, the relation between F and α can be simulated by a linear function Eq. (C3).

$$\alpha = \alpha_{threshold} + k_3\left(F - F_{threshold}\right) \tag{C3}$$

where $F_{threshold}$ is the driving force corresponding with $\alpha_{threshold}$, through Eq. (24). In this case, $\alpha_{threshold}$ is set to be 0.1, and the value for k_3 calibrated from Fig. B1 is $k_3 = 4.4\times10^{-7}$.

The final modeling result for plant tissue is shown in Fig. C2 below. Fig. C2 shows similar modeling result with Figure 5, where the relation between α and F is modeled by the Preisach-Krasnoselskii operator.

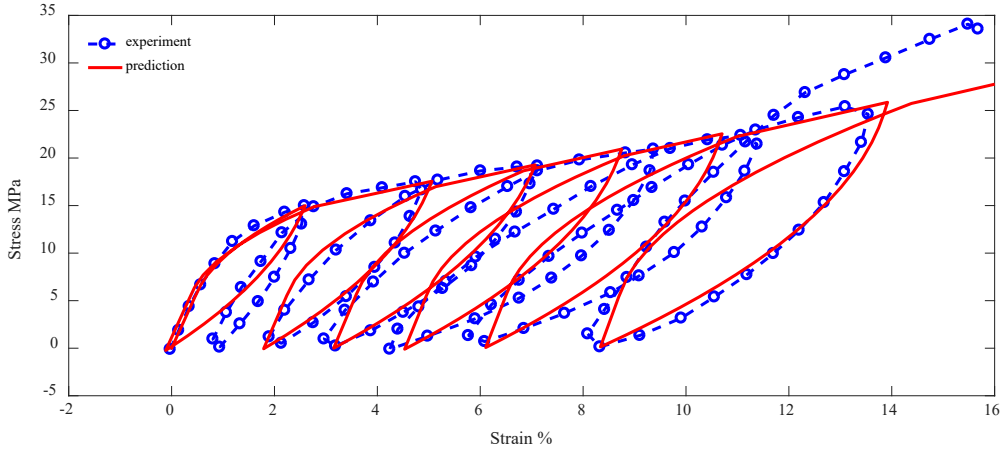

Figure C2 Modeling result for plant tissue